 CMES, vol.14, no.2, pp.119-128, 2006

The Applications of Meshless Local Petrov-Galerkin (MLPG) Approaches in High-Speed Impact, Penetration and Perforation Problems

Z. D. Han[1], H. T. Liu[1], A. M. Rajendran[2], S. N. Atluri[3]

Abstract: This paper presents the implementation of a three-dimensional dynamic code, for contact, impact, and penetration mechanics, based on the Meshless Local Petrov-Galerkin (MLPG) approach. In the current implementation, both velocities and velocity-gradients are interpolated independently, and their compatibility is enforced only at nodal points. As a result, the time consuming differentiations of the shape functions at all integration points is avoided, and therefore, the numerical process becomes more stable and efficient. The ability of the MLPG code for solving high-speed contact, impact and penetration problems with large deformations and rotations is demonstrated through several computational simulations, including the Taylor impact problem, and some ballistic impact and perforation problems. The computational times for the above simulations are recorded, and are compared with those of the popular finite element code (Dyna3D), to demonstrate the efficiency of the present MLPG approach.

keyword: Meshless method, MLPG, High-speed impact, Penetration

1 Introduction

With the dramatically increased high-performance computational power, computational mechanics has become an important tool in both civilian and military system design and analysis. Although the finite element method (FEM), as the most recognized approach, has achieved a phenomenal success, accurate and efficient numerical simulations of armor/anti-armor systems is still a challenging task, due to the fact that these applications always involve high strain rate, non-linear deformation and severe element distortion. Recently, a great effort has been put into this field. Johnson et al (2003) proposed an "element to particle" conversion method to alleviate the problem of highly distorted meshes in fracture and fragmentation problems. This mixed mesh/particle method seems to provide stable and useful solutions to several impact problems; however, these types of numerical approaches tend to remain "phenomenological", and are limited to a small class of problems. Ortiz and his colleagues developed FEM based fracture and fragmentation algorithms, in which cohesive zones are assumed between element boundaries, and cracks can be propagated between the elements using cohesive laws [Ortiz and Pandolfti (1999)]. They used advanced nonlinear error estimation and non smooth contact algorithms to assure numerical accuracy and stability. Unfortunately, this advanced FEM approach seems to suffer from mesh-influenced solutions. In addition, these element-based approaches require a tremendous effort in generating good quality meshes for complex geometrics, and for component assemblies.

In contrast, the meshless methods have become very attractive for eliminating the mesh distortion problems due to large deformations. Some meshless methods are based on the global weak forms, such as the smooth particle hydrodynamics (SPH), and the element-free Galerkin methods (EFG). They may require a certain node distribution pattern, or background cells for integration, which may be not lead to satisfactory solutions when meshes are severely distorted during large deformations. In addition, in the usual meshless approaches, the shape functions are generally very complicated, which results in even more complicated derivatives. Thus, the accurate calculation of the shape function derivatives is always a time-consuming task, and many more Gaussian points are required in the domain integration. The high computational expense and complexity is a barrier that prevents the application of meshless method to large-scale simulations. Most of the current meshless codes and applications are restricted to two-dimensional demonstrations.

Recently, Atluri and his colleagues [Atluri and Zhu

[1] Knowledge Systems Research, LLC, Forsyth, GA 30253
[2] US Army Research Office (ARO), RTP, NC
[3] Center for Aerospace Research & Education, University of California, Irvine

(1998), Atluri and Shen (2002), and Atluri (2004)] proposed a general framework for developing the Meshless Local Petrov-Galerkin (MLPG) approach, which provides flexibility in choosing the local weak forms, the trial functions, and the independent test functions for solving systems of partial differential equations. The MLPG approach has the following advantages: (1) all weak forms are formulated locally; (2) various trial and test functions can be chosen and combined together for solving one problem; (3) overlapping local sub-domains can be chosen in such a way as to match problems and algorithms in any special cases. The flexibility in choosing and combining various trial and test functions make the simplification of meshless formulation possible. For example, by choosing the heavy-side function (a unity-valued function inside the sub-domain, and zero outside the sub-domain), the domain integration is eliminated and the local symmetric weak form is expressed as a boundary integration. This will reduce the number of integration points, and greatly increase the accuracy and efficiency. In the MLPG method, the equilibrium and energy conservation equations are written locally within the subdomains, which make the parallel computation straightforward. As an extension, a meshless mixed finite volume method is proposed [Atluri, Han and Rajendran (2004), Han, Rajendran and Atluri (2005)] to further simplify the meshless formulations. In the MLPG mixed method, the displacement-/velocity- gradients are interpolated independently from the displacement/velocity interpolations. The compatibility between the displacements/velocities and displacement-/velocity-gradients is enforced only at nodal points. The mixed MLPG does not require the calculation of the derivatives of the complex shape functions, and thus achieves more computational accuracy and efficiency. It should be pointed out that the MLPG mixed method is radically and fundamentally different from the finite-element mixed method, which is a saddle point variational problem and which is often plagued by the stability conditions such as the Brezzi-Babuska conditions(Xue , Karlovitz, and Atluri(1985).

In the present paper, the above described MLPG mixed method is implemented in an explicit-time-integration computational code, with an updated Lagrangean description. For completeness purpose, a brief description of the MLPG mixed method is presented in the following section. Several numerical examples are presented to show the applicability of the meshless program.

2 MLPG Formulation

2.1 Local Nodal Interpolation

An appropriate meshless interpolation scheme should satisfy the *locality*, *continuity*, and *consistency* requirements. Among a variety of local interpolation schemes, the Moving Least Squares (MLS) interpolation is generally considered to be one of the best schemes to interpolate random data with a reasonable accuracy, because of its completeness, robustness and continuity. With the MLS, a trial function $u(\mathbf{x})$ can be expressed as

$$u(\mathbf{x}) = \sum_{I=1}^{N} \Phi^I(\mathbf{x})\hat{u}^I \tag{1}$$

where $\hat{u}^I$ and $\Phi^I(\mathbf{x})$ are the fictitious nodal values, and the shape function of node I, respectively. The shape functions are obtained by minimizing the L_2 norm of the weighted distance between the trial function value and its true values at nodal points. For a detailed derivation and explicit expressions for the shape functions, the readers are referred to Atluri (2004).

The MLS nodal shape function $\Phi^I(\mathbf{x})$ has a rational form, and it is non-zero only inside the support domain of its corresponding node I. We define the nodes whose support domain covers $\mathbf{x}$ as the neighbor node of $\mathbf{x}$. The trial function $u(\mathbf{x})$ is only relying on its immediate neighbors' nodal values and thus the *locality* is preserved. The smoothness of the shape function $\Phi^I(\mathbf{x})$ is determined by its basis functions and the weight functions. Therefore, it is easy for the MLS approximation to yield a high-order *continuity* for the shape functions and then the trial functions. In practice, polynomials are adopted as the basis functions and spline functions as the weight functions. Therefore, to construct a more continuous shape function will be a trivial task. The MLS interpolation constructed in Eq. (1) is able to represent the jth (j=1,2, ... m, with m is the number of the polynomial basis functions) component of monomials exactly. In other words, the shape function is consistent.

In the mixed method, we interpolate the velocities v_i and velocity gradients $v_{i,j}$ independently using the same shape functions, namely

$$v_i(\mathbf{x}) = \sum_{J=1}^{N} \Phi^J(\mathbf{x})v_i^J \tag{2}$$

$$v_{i,j}(\mathbf{x}) = \sum_{K=1}^{N} \Phi^K(\mathbf{x}) v_{i,j}^K \tag{3}$$

The compatibility condition between the velocities and velocity gradients is enforced only at the nodes by a standard collocation method as

$$v_{i,j}(\mathbf{x}^I) = \frac{\partial v_i(\mathbf{x}^I)}{\partial x_j} \tag{4}$$

By interpolating the velocity gradients, as one of the key features of the mixed method, we eliminate the differentiation operations of the shape functions in the local weak form integration. Therefore, the requirement of the completeness and continuity of the shape functions is reduced by one-order, and thus, lower-order polynomial terms can be used in the meshless approximations. This leads to a smaller nodal influence size and speeds up the calculation of the shape functions. The adoption of the mixed method in our implementation greatly improves the program efficiency.

2.2 Formulations for Finite Strain Problems

Since the purpose of the developed MLPG program is to simulate high-speed dynamic problems, we adopted an updated Lagrangian formulation in our implementation. Let x_i be the spatial coordinates of a material particle in the current configuration. Let $\dot{S}_{ij}$ be the Truesdell stress-rate (the rate of second Piola-Kirchhoff stress as referred to the current configuration); and let $\mathring{\sigma}_{ij}^J$ be the Jaumann rate of Kirchhoff stress (which is J times the Cauchy stress, where J is the ratio of volumes). It is known [Atluri (1980)]:

$$\dot{S}_{ij} = \mathring{\sigma}_{ij}^J - D_{ik}\sigma_{kj} - \sigma_{ik}D_{kj} \tag{5}$$

Here, D_{ij} and W_{ij} are the symmetric and skew-symmetric parts of the velocity gradient, respectively. Considering a 3D domain Ω with a boundary $\partial\Omega$, the rate forms of the linear and angular momentum balances are [Atluri (1980)]:

$$(\dot{S}_{ij} + \tau_{ik}v_{j,k})_{,i} + \dot{f}_j = \rho\dot{a}_j \tag{6}$$

where, ρ is the mass density and $\dot{a}_j$ the acceleration rate. In a dynamic problem, $\dot{f}_j$ are appropriately defined in terms of the rate of change of inertia forces and $(\,)_{,i} = \partial(\,)/\partial x_i$; x_i are current coordinates of a material particle. In Eq. (6), τ_{ij} is the Cauchy stress in the current configuration.

2.3 Local weak form with the large deformations

In the MLPG approaches, the weak form is established over a local subdomain Ω_s, which may have an arbitrary shape and contain a point $\mathbf{x}$ in question. In our implementation, the local weak form is established for a spherical subdomain with the radius of r (we define it as the test-function size), namely

$$\int_{\Omega_s} [(\dot{S}_{ij} + \tau_{ik}v_{j,k})_{,i} + \dot{f}_j - \rho\dot{a}_j] w_j d\Omega = 0 \tag{7}$$

where w_j are the test functions. By applying the divergence theorem Eq. (7) may be rewritten in a symmetric weak form as:

$$\int_{\partial\Omega_s} (\dot{S}_{ij} + \tau_{ik}v_{j,k}) n_i w_j d\Gamma - \int_{\Omega_s} [(\dot{S}_{ij} + \tau_{ik}v_{j,k}) w_{j,i} - \dot{f}_j w_j + \rho\dot{a}_j] d\Omega = 0 \tag{8}$$

with the rate definition $\dot{t}_j = (\dot{S}_{ij} + \tau_{ik}v_{j,k})n_i$, and with n_i being the components of a unit outward normal to the boundary of the local subdomain Ω_s, in its current configuration. Thus the local symmetric weak form can be rewritten as

$$\int_{L_s} \dot{t}_i w_i d\Gamma + \int_{\Gamma_{su}} \dot{t}_i w_i d\Gamma + \int_{\Gamma_{st}} \dot{\bar{t}}_i w_i d\Gamma - \int_{\Omega_s} [(\dot{S}_{ij} + \tau_{ik}v_{j,k}) w_{j,i} - \dot{f}_i w_i + \rho\dot{a}_j] d\Omega = 0 \tag{9}$$

where Γ_{su} is a part of the boundary $\partial\Omega_s$ of Ω_s, over which the essential boundary conditions are specified. In general, $\partial\Omega_s = \Gamma_s \cup L_s$, with Γ_s being a part of the local boundary located on the global boundary, and L_s is the other part of the local boundary which is inside the solution domain. $\Gamma_{su} = \Gamma_s \cap \Gamma_u$ is the intersection between the local boundary $\partial\Omega_s$ and the global displacement boundary Γ_u; $\Gamma_{st} = \Gamma_s \cap \Gamma_t$ is a part of the boundary over which the natural boundary conditions are specified.

To simplify the integration and speed up the numerical implementation, the Heaviside function is adopted as the test function in our program program(Thus, the method is labeled here as the " finite-volume" MLPG method). Thus, the local symmetric weak form in Eq.(9) becomes

$$-\int_{L_s} \dot{t}_i d\Gamma - \int_{\Gamma_{su}} \dot{t}_i d\Gamma + \int_{\Omega_s} \rho\dot{a}_j d\Omega = \int_{\Gamma_{st}} \dot{\bar{t}}_i d\Gamma + \int_{\Omega_s} \dot{f}_i d\Omega \tag{10}$$

This equation has the physical meaning that it represents the balance law of the local sub-domain Ω_s, as in conventional finite volume methods.

3 Numerical Implementation

In this section, we will address some numerical issues in the implementation of the MLPG mixed method.

3.1 Determination of the Support Sizes

The support size is an important parameter in the MLPG calculation. On the one hand, the support size should be large enough to include enough neighboring nodes to ensure the regularity and reduce the computational error; on the other hand, we should keep the support size relatively small to maintain the interpolation's locality. In the current implementation, the support size for each node is determined automatically from the neighbor nodes, on demand.

To ensure the regularity of the MLS interpolation, the minimum number of the linearly independent neighbor nodes is decided by the order of the polynomial basis. For the three-dimensional problems, the neighbor node number m is calculated from the order of the polynomial basis t as [Atluri (2004)]

$$m = (t+1)(t+2)(t+3)/6 \tag{11}$$

Eq. (11) means that for each point $\mathbf{x}$, it is required that there are m neighbor nodes whose support domains cover the point $\mathbf{x}$. On other words, for a node J, its support size should be large enough to cover all the nodes, of which the node J is a neighbor node. To increase the efficiency of the present implementation, the support sizes are not recalculated for each time step. Therefore, a scale factor, which is great than 1, is applied to the support sizes decided by the above procedure, to account for the effect of the nodal movement from the body's deformation.

3.2 Determination of the Test Sizes

The test domains in the MLPG could be any overlapping local domains. A spherical domain centered at each node is adopted in the present implementation. For a node I, the radius of the spherical domain (the test size) is determined as

$$r_0^I = \alpha \min\left\{\left\|\mathbf{x}^I - \mathbf{x}^J\right\|\right\}, \quad J = 1,2,...,N \text{ and } I \neq J \tag{12}$$

where α is the scale factor of the test size, which is a constant between 0 and 1. In addition, if node I is inside the solution domain, but close to the global boundary, a smaller radius may be used so that the local sphere has no intersection with the global boundary. In other words, the local test domains of all internal nodes are restricted to be inside the solution domain, and their local boundaries are also inside the solution domain. Therefore, the numerical implementation becomes much simpler, because the essential and natural boundary conditions appear in the integrals of the nodes on the global boundary only.

3.3 Numerical Quadrature

In the present implementation, the integrations of the local symmetric weak form [Eq. (10)] are performed numerically by using the conventional Gaussian quadrature scheme. The boundary integration in Eq. (10) over a spherical surface involves the trigonometric functions. It is well known that the conventional numerical quadrature schemes are designed for polynomials, and are not efficient for trigonometric or rational functions. To improve the performance of the numerical integration, the local subdomain (i.e. a sphere) is partitioned by triangles for the surface integration [Han and Atluri (2004)].

3.4 Time Integration

The well known and commonly accepted Newmark β method [Newmark (1959)] is used in the present implementation to integrate the governing equations in time. With the determined accelerations from the system equations based on the local symmetric weak form [Eq. (10)], the displacements and velocities are calculated from the standard Newmark β method as

$$\mathbf{u}^{t+\Delta t} = \mathbf{u}^t + \Delta t \mathbf{v}^t + \frac{\Delta t^2}{2}\left[(1-2\beta)\,\mathbf{a}^t + 2\beta \mathbf{a}^{t+\Delta t}\right]$$

$$\mathbf{v}_c^{t+\Lambda t} = \mathbf{v}^t + \Delta t\left[(1-\gamma)\,\mathbf{a}^t + \gamma \mathbf{a}^{t+\Delta t}\right] \tag{13}$$

For zero damping system, this method is unconditionally stable if

$$2\beta \geq \gamma \geq \frac{1}{2} \tag{14}$$

and conditionally stable if

$$\gamma \geq \frac{1}{2}, \quad \beta \leq \frac{1}{2} \text{ and } \Delta t \leq \frac{1}{\omega_{\max}\sqrt{\gamma/2-\beta}} \tag{15}$$

where $\omega_{\max}$ is the maximum frequency in the structural system.

This method can be used in the predictor-corrector mode, with specified initial conditions [Atluri (2004)]. In the present implementation, the central difference scheme is used by setting $\beta = 0$ and $\gamma = 1/2$.

4 Ceramic Constitutive Model with Damage

In the present implementation, the Rajendran and Grove (RG) ceramic damage model is adopted to model the material damage and failure during the impact and penetration process. The RG ceramic model [Rajendran (1994); Rajendran and Grove (1996)] is a sophisticated, three-dimensional, internal-state-variable-based constitutive model for ceramic materials, which incorporated both micro-crack propagation and void collapse. The proposed RG ceramic damage model has achieved a great success in describing the response of alumina (AD85) subjected to various stress/strain loading conditions [Rajendran (1994)]. In this section, the RG ceramic damage model is briefly reviewed and the main formulation is presented for completeness purposes.

4.1 Constitutive Relationships

In the RG model, the total strain $\varepsilon_{ij}$is decomposed into the elastic part ε^e_{ij} and plastic part ε^p_{ij}. The pressure is calculated through the Mie-Gruneisen equation of state as

$$P = \left[\overline{P}_H\left(1-0.5\Gamma\overline{\eta}\right)+\Gamma\rho_0\left(I-I_0\right)\right] \tag{16}$$

with

$$\overline{P}_H = K_\gamma\left(\beta_1\overline{\eta}+\beta_2\overline{\eta}^2+\beta_3\overline{\eta}^3\right) \tag{17}$$

In the above equations, β_1, β_2 and β_3 are empirical parameters; Γ is the Mie-Gruneisen parameter; $K_\gamma = \overline{K}/K$ is the bulk modulus reduction ratio, with K being the bulk modulus for the intact matrix and $\overline{K}$ the effective bulk modulus for the micro-crack containing material. Furthermore, ρ_0 is the initial material density; I_0 and I are the internal energy at the initial and current states, respectively. The engineering volumetric strain, with the consideration of the voids, is defined as

$$\overline{\eta} = \frac{(1-f_0)V_0}{(1-f)V} - 1 \tag{18}$$

Where V_0 and V are the volumes of the initial and current states; f_0 and f are the initial and current porosity densities, respectively.

The deviatoric stress is related with the deviatoric elastic strain e^e_{ij} as

$$S_{ij} = 2R_g\overline{G}e^e_{ij} \tag{19}$$

Here $\overline{G}$ is the effective shear modulus for micro-crack containing material and R_g is the correction factor for shear modulus due to the existence of porosity, which is given in Rajendran and Grove' paper (1996). The porosity density is assumed to decrease due to void collapsing at pressures above the HEL as

$$\dot{f} = (1-f)\,\dot{\varepsilon}^p_v \tag{20}$$

with ε^p_v the plastic volumetric strain and the dot means the temporal derivative.

When the materials are shocked above the HEL (Hugoniot Elastic Limit), plastic flow occurs. In the current model, Gurson's pressure dependent yield function, with considerations of the porosity, is adopted, namely

$$F = \frac{3J_2}{Y^2} + 2f\cosh\left(\frac{3P}{2Y}\right) - f^2 - 1 = 0 \tag{21}$$

with $J_2 = 0.5S_{ij}S_{ij}$. A simplified Johnson-Cook strain rate dependent strength model is used and can be expressed as

$$Y = C_1\left(1 + C_3\ln\frac{\dot{\varepsilon}_p}{\dot{\varepsilon}_0}\right) \tag{22}$$

where C_1 and C_3 are model constants. $\dot{\varepsilon}_p$ is the equivalent plastic strain rate and $\dot{\varepsilon}_0$ is the reference strain rate, which is assumed to be 1 in the current model.

4.2 Damage Definition and Evolution

The micro-crack damage is measured in terms of a dimensionless micro-crack damage density γ, which is expressed as

$$\gamma = N^*_0 a^3 \tag{23}$$

where N^*_0 is the average number of micro-flaws per unit volume and a is the maximum micro-crack size at the

current state. The initial values of N_0^* and a_0 are material constants. For simplicity, it is assumed that there is no crack nucleation during the loading, and therefore the damage evolution is represented by the growth of micro-crack size a, which follows a generalized Griffith criterion, as

$$\dot{a} = \begin{cases} 0 & G_s \le G_C \\ n_1 C_R \left[1 - \left(\frac{G_C}{G_S}\right)^{n_2}\right] & G_s > G_C \end{cases} \tag{24}$$

where C_R is the Rayleigh wave speed, G_C is the critical strain energy release rate for micro-crack growth calculated from the fracture toughness K_{IC}, Young's modulus E and Poisson's ratio v as $G_C = K_{IC}^2\left(1-v^2\right)/E$. G_S is the applied strain energy release rate. n_1 and n_2 are the parameters controlling the crack growth rate. Four parameters are used for the micro-crack extension model: n_1^- and n_2^- for crack sliding, and n_1^+ and n_2^+ for crack opening.

4.3 Pulverization

When the micro-crack damage density γ reaches a critical value (usually set as 0.75) under compressive loading, the material becomes pulverized. The bulk and shear moduli for the pulverized material are set to the corresponding effective bulk and shear moduli at the pulverization point. The pulverized material does not support any tensile loading and the compressive strength of the pulverized material is described by the Mohr-Columb law as

$$Y = \begin{cases} 0 & ,P \le 0 \\ \alpha + \beta P & ,P > 0 \end{cases} \tag{25}$$

where α and β are model constants. The pressure is simply computed from the elastic volumetric strain ε_v^e as

$$P = \begin{cases} 0 & ,\varepsilon_v^e \ge 0 \\ -\overline{K}_p \varepsilon_v^e & \varepsilon_v^e < 0 \end{cases} \tag{26}$$

4.4 Determination of Model Constants

In the Rajendran-Grove ceramic model, there are eight material constants to describe the micro-crack behavior: N_0^*, a_0, μ, n_1^+, n_2^+, n_1^-, n_2^-, and K_{IC}. Usually, several experiments such as the plate-on-plate and the bar-on-bar impact tests are needed to determine these constants for a specific material. Rajendran and Grove (1996) conducted a sensitivity study of the material constants, and calibrated the constants for several commonly used ceramic materials, like SiC, B_4C, TiB_2, AD85, and AD995. In the following numerical simulations, the AD85 ceramic is used and the material constants that we employed are listed in Table 1.

Table 1 : The material constants for Rajendran-Grove model

	AD85
Density (g/cm^3)	3.42
Shear Modulus (GPa)	88.0
Initial Porosity	10%
Material Strength Constants	
C_1 (GPa)	4.0
C_3	0.029
Equation of State Constants	
β_1 (GPa)	150.0
β_2 (GPa)	150.0
β_3 (GPa)	150.0
Γ	0
Damage Model Parameters	
N_0^* (m^{-3})	1.83×10^{10}
a_0 (μm)	0.58
μ	0.72
n_1^+	1.0
n_2^+	0.07
n_1^-	0.1
n_2^-	0.07
K_{IC} ($MPa\sqrt{m}$)	3.25
Pulverized Material Constants	
α (GPa)	0.1
β	0.1

5 Numerical Examples

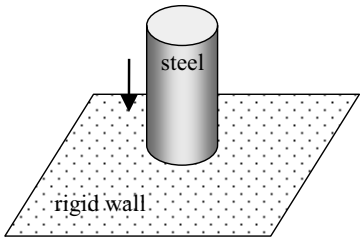

Figure 1 : Taylor's problem: a solid cylinder impacting a rigid surface

Two numerical examples are presented here to show the applicability of the developed MLPG program in solv-

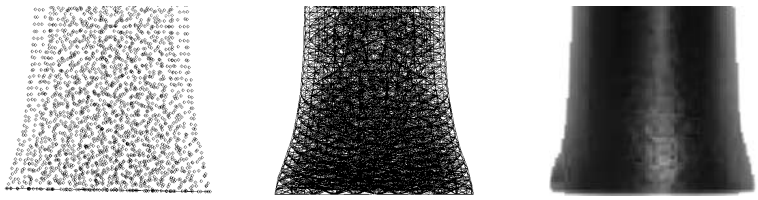

Figure 2 : Deformed profile of the cylinder at 50 micro-seconds: (a) MLPG mixed method; (b) Finite element model; and (c) Test

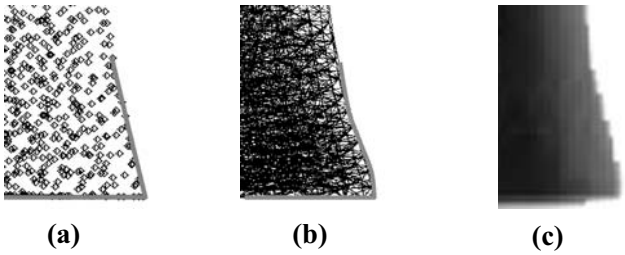

Figure 3 : The lower corner of the deformed profile at 50 micro-seconds: (a) MLPG mixed method; (b) Finite element model; and (c) Test

ing contact, impact, penetration and perforation problems with large deformation. For the sake of readability and brevity, the details of the implementation of the MLPG contact, penetration, and perforation algorithms are omitted here, and will be reported elsewhere.

5.1 Taylor Impact Problem

The Taylor test is often used to determine the dynamic yield stress of a material in a state of uniaxial stress. The Taylor impact problem can simply be described as a solid cylinder impacting a rigid surface in the normal direction, shown in Figure 1. In the present study, a cylinder with a length of 12.7 cm and a radius of 76.2 cm is impacting a rigid surface with an initial impact velocity of 300 m/s. The solid cylindrical rod is modeled as being elasto-plastic, and the material is chosen as AISI 310 steel with the following material constants: density: 8.027 g/cm^3, Young's modulus: 199.95 GPa, Poisson's ratio: 0.28, yield strength: 310.26 MPa, and 1% hardening slope : 2.0 GPa.

This Taylor impact problem is simulated using the present MLPG program. For comparison purposes, the finite element code Dyna3D (version 2000) is also used to analyze this problem, using the mesh generated from the same nodal configuration. The top surface of the cylinder reaches the lowest point at about 50 micro seconds. The deformed profile of the cylinder is shown in Fig. 2(a) using the MLPG mixed method and in Fig. 2(b) using Dyna3D. Both codes give similar profiles. However, the MLPG method gives a straight corner while Dyna3D gives a curved one, for this *frictionless contact* impact. The corners of the deformed profiles are enlarged in Table 1.

In analyzing this problem, the present MLPG mixed method is used without any hour-glass control, or any other artificial numerical treatments. In contrast, one-point Gauss integration scheme is used in Dyna3D, along with hour-glass control. The total CPU times for the straightforward MLPG mixed method, and the Dyna3D with hour-glass control and artificial viscosity, are almost same. It clearly demonstrates the superior performance of the present MLPG mixed method as compared to the FEM methods.

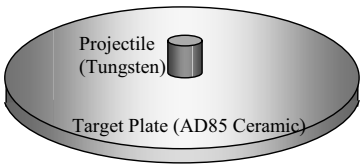

Figure 4 : Ballistic impact test configuration schematic

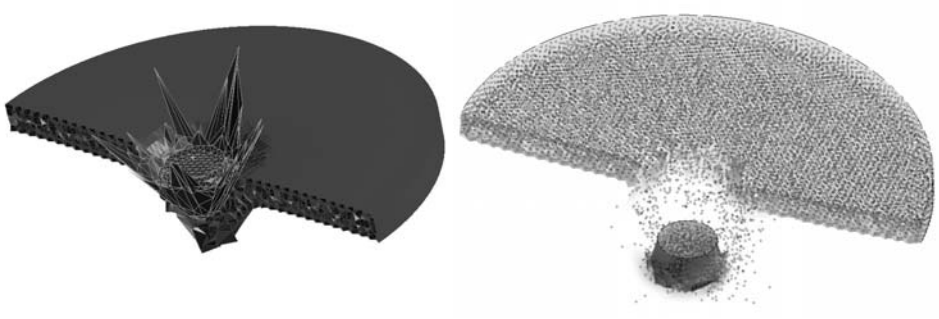

(a) Dyna3D Results
(failed after 8 micro-seconds)

(b) MLPG Results
(complete peneration after 19 micro-seconds)

Figure 5 : Ballistic Impact Penetration

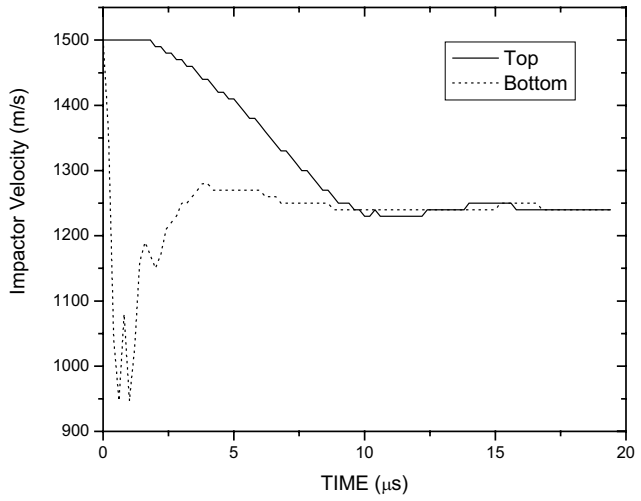

Figure 6 : Remaining speed of the projectile after penetration

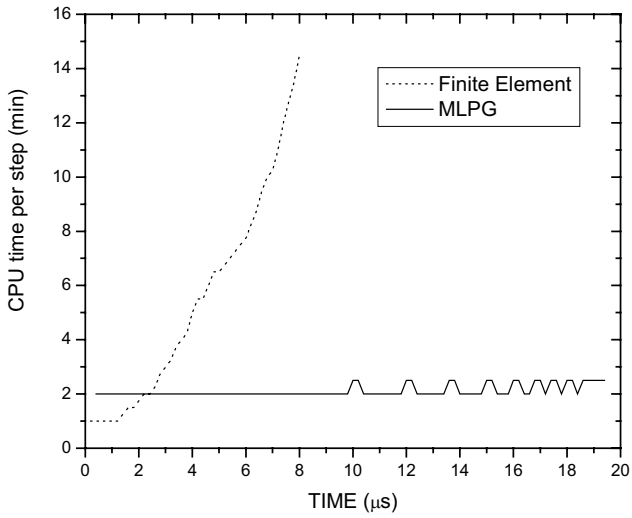

Figure 7 : CPU time comparson between MLPG and finite element apporaches

5.2 Ballistic Impact

In this simulation, we consider a cylindrical tungsten projectile to impact with an AD85 ceramic plate at the velocity of 1500 m/s. Both the length and diameter of the projectile are 10 mm. The target ceramic plate has a thickness of 5 mm and a diameter of 80 mm. Fig. 3 shows the experimental configuration. The tungsten is modeled as being elastoplastic, with the following material properties: density 16.98 g/cm^3, Young's modulus 299.6 GPa, Possion's ratio 0.21 and yield strength 1.5 GPa. The target plate is modeled using the Rajendran-Grove ceramic damage model, which was implemented into the present MLPG implementation, as well as in Dyna3D.

The simulation using finite element method (Dyna3D) stops at 8 micro-seconds due to severe element distortion, as shown in Figure 4(a). The *total simulation time with Dyna3D is over 5 hours*. As pointed out by Johnson and Robert (2003), the Lagrangian finite element algorithms are not always adequate when the distortions become very severe. The meshless method, which could be used to represent severe distortions in a Lagrangian framework, is more suitable to simulate the problems with severe distortions like ballistic penetration.

The same problem is re-simulated by using the MLPG method; and it is solved smoothly without any mesh distortion problems, because of the advantages of the truly meshless method. The total solution time is 20 micro-seconds, and *it takes about 1 hour for the first 8 micro-*

seconds, and 2.5 hours to carry out the whole analysis. The final deformation is shown in Figure 4(b), and the fragmentation is clearly formed after the projectile penetrates the target plate. The steady remaining speed of the projectile is about 1240 m/s after impact, with the velocity history chattered in Fig. 4. In addition, the MLPG method is more stable than the FEM as a steady CPU time is demonstrated during the whole solution time. However, the FEM is encountering a severe mesh distortion problem, and CPU time jumps up once the projectile and plate are undergoing the large deformation right after a few micro seconds of the solution time, shown in Fig. 5.

6 Closing Remarks

The meshless method has been a very active research area for over ten years in the computational mechanics field. However, due to the intrinsic complexity of the approach, most of the research is still at the academic level. The MLPG method, as a meshless framework, provides the flexibility to construct various meshless approaches by different choices and combinations of the trial and test functions; therefore, provides the possibility to simplify the numerical procedure and lead to an efficient and stable meshless implementation.

The present development of software is based on the MLPG mixed finite volume method for solving three-dimensional nonlinear problems. The MLS approximations are used for both velocity and velocity-gradients interpolations, independently. The adoption of the Heaviside function as the test function eliminates the domain integration in the local weak form. In addition, the support size and test size are determined automatically by the program based on the nodal density and distribution. All of these efforts lead to a high-performance MLPG dynamic program, which shows the potential to replace the finite element method in some computational areas, such as solving the high-speed impact and penetration problems. These potentials are demonstrated through the two numerical examples. The 3D Taylor-impact example demonstrates that the present mixed method possesses an excellent accuracy and efficiency, as compared to the FEM. *The present method requires no special numerical treatments to handle the nonlinear static and dynamic problems, such as the reduced integration, hourglass control, and so on*. The ballistic-impact and perforation example demonstrates the ability of the MLPG mixed method in solving high-speed problems with severe distortion and fragmentation. Compared with FEM, the MLPG is not only more stable but also more efficient.

References

Atluri, S. N. (1980): On some new general and complementary energy theorems for the rate problems of finite strain, classical elastoplasticity. *Journal of Structure and Mechanics*, vol. 8, pp. 61-92.

Atluri, S.N (2004): *The Meshless Local Petrov-Galerkin (MLPG) Method for Domain & Boundary Discretizations*, Tech Science Press, 665 pages.

Atluri S.N., Shen S.P. (2002): The meshless local Petrov-Galerkin (MLPG) method: A simple & less-costly alternative to the finite element and boundary element methods, *CMES: Computer Modeling in Engineering and Sciences*, 3 (1) 11-51

Atluri, S. N.; Han, Z. D.; Rajendran, A. M. (2004): A New Implementation of the Meshless Finite Volume Method, Through the MLPG "Mixed" Approach, *CMES: Computer Modeling in Engineering & Sciences*, vol. 6, no. 6, pp. 491-514.

Atluri, S. N.; Zhu, T. (1998): A new meshless local Petrov-Galerkin (MLPG) approach in computational mechanics. *Computational Mechanics*, Vol. 22, pp. 117-127.

Han. Z. D.; Atluri, S. N. (2004): Meshless Local Petrov-Galerkin (MLPG) approaches for solving 3D Problems in elasto-statics, *CMES: Computer Modeling in Engineering & Sciences*, vol. 6 no. 2, pp. 169-188.

Han Z. D.; Rajendran, A. M; Atluri, S. N. (2005): Meshless Local Petrov-Galerkin (MLPG) Approaches for Solving Nonlinear Problems with Large Deformation and Rotation, *CMES: Computer Modeling in Engineering & Sciences*, vol. 10, no. 1, pp. 12.

Johnson, G.R.; Robert, A.S. (2003): Conversion of 3D Distorted Element into Meshless Particles During Dynamic Deformation. *Int. J. Impact Engng.*, vol. 28, pp. 947-966.

Johnson, G. R.; Stryk, R. A. (2003): Conversion of 3D distorted elements into meshless particles during dynamic deformation, *International Journal of Impact Engineering*, vol. 28, pp. 947–966.

Newmark, N. M. (1959): A method of computation for structural dynamics, *Journal of the Engineering mechan-*

ics Division, ASCE, vol. 86, pp. 67-95.

Ortiz, M.; Pandolfi, A. (1999): Finite-Deformation Irreversible Cohesive Eelemnts for Three-Dimensional Crack-Propagation Analysis, *International Journal for Numerical Methods in Engineering*, Vol. 44, pp. 1267-1282.

Rajendran, A.M. (1994): Modeling the Impact Behavior of AD85 Ceramic under Multiaxial Loading. *Int. J. Impact Engng.*, Vol. 15, No. 3, pp. 749-768.

Rajendran, A. M.; Grove, D.J. (1996): Modeling the Shock Response of Silicon Carbide, Boron Carbide and Titanium Diboride. *Int. J. Impact Engng.*, Vol. 18, No. 6, pp. 611-631.

Xue, W.-M., Karlovitz, L. A., and Atluri, S.N(1985): On the Existences and Stability Conditions for Mixed-Hybrid Finite Element Solutions Based on Reissner's Variational Principle, *International Journal of Solids and Structures*, Vol. 21(1), pps. 97-116,